applied sciences

MDPI

Article

Design of a Spin Test System for Burst Phenomen Considering Nonlinear Rotordynamic Effects

Mert Uğur * and Osman Kopmaz

Department of Mechanical Engineering, Bursa Uludağ University, 16059 Bursa, Turkey; okopmaz@uludag.edu.tr
* Correspondence: mertugur1993@gmail.com; Tel.: +90-5345655881

Abstract: This study presents the development and evaluation of a spin test rig for high-speed rotating components. The innovation of this study is using a discrete model to determine dynamic positioning during the preliminary design phase based on vibration characteristics. The primary aim is to manage vibrations and alternating stress effects from rotor dynamics to prevent issues such as crack propagation or bursts before achieving desired speeds. MATLAB 2023b Simulink-based tool was developed, which played a role in providing the design of bearing support regions and stiffness values. The system underwent rigorous validation through structural, modal, and harmonic finite element analyses. Testing showed a maximum deviation of 4.2% for 10 kg specimen and 4.85% for 4 kg specimen between Simulink predictions and actual data, due to factors such as contact and bearing damping. For the 10 kg specimen, the maximum equivalent stress was 314.92 MPa with an alternating stress of 64.87 MPa at 0.5% damping ratio, representing 37.27% of the yield limit. For the 4 kg specimen, the maximum equivalent stress was 513 MPa with alternating stress below 40 MPa at 3% damping ratio, corresponding to 54.32% of the yield limit. This research enhances the reliability and performance of high-speed rotating machinery.

Keywords: spin test rig; alternating stress; rotor dynamics; finite element analyses

check for updates

Citation: Uğur, M.; Kopmaz, O. Design of a Spin Test System for Burst Phenomen Considering Nonlinear Rotordynamic Effects. *Appl. Sci.* **2024**, *14*, 9399. https://doi.org/10.3390/app14209399

Academic Editor: Yves Gourinat

Received: 15 September 2024
Revised: 1 October 2024
Accepted: 11 October 2024
Published: 15 October 2024

Copyright: © 2024 by the authors. Licensee MDPI, Basel, Switzerland. This article is an open access article distributed under the terms and conditions of the Creative Commons Attribution (CC BY) license (https://creativecommons.org/licenses/by/4.0/).

1. Introduction

Spin test rigs are systems used to test the dynamic phenomena and structural strength limits of components operating at high speeds [1,2]. The purpose of the applications carried out in the test rig is to examine phenomena such as plastic deformation, crack propagation, and burst by rotating the part under test at high angular speeds and exposing it to centrifugal load [3]. Tests can be performed under vacuum and at high temperatures, depending on the operating conditions of the test rig. Components operating at high speeds, such as turbines and compressors of gas turbine engines, high-speed gears, and rotating parts of turbochargers and centrifugal pumps, can be tested under maximum load conditions in spin test rigs [4–8]. During the test stages, the aim is to expose the disc structure to burst by accelerating to the targeted speeds. However, before the disc bursts, plastic deformation will occur in the material. This associated plastic deformation will cause crack propagation [9,10]. The burst phenomenon will occur as the crack size increases and the disc continues to be exposed to centrifugal force. The spin test rigs operate under vacuum and are driven by an electric motor running at high speeds for structures with a low inertia tensor [11–15]. The most important reason for operating the system under vacuum is to reduce the aerodynamic torque to zero, making electric motor selection easier and eliminating aerodynamic effects during the test. With vacuum, both aerodynamic damping is eliminated and convective heat transfer is prevented [16–19]. In this way, a temperature gradient is achieved on the part. Without a vacuum, it would be almost impossible to capture the temperature gradient on the test specimen, which would be exposed to convective heat transfer [20–22].

It is crucial that the spin test system operates smoothly in terms of rotor dynamics [23]. The most important factor here is ensuring that any natural frequency of the part, shaft, or assembly does not resonate at a speed close to the test speed [24–27]. If such a situation occurs, suitable test conditions may be disrupted. Particularly, when examining the natural frequencies obtained from the entire assembly of the part to be tested, it is essential that there is no critical speed in the range corresponding to ±20% of the test RPM [28,29]. For these reasons, detailed modal analysis must be performed, and the part test range must be kept away from rotor dynamic effects [30,31].

This study conducted in [32] highlights the importance of flywheel strength in energy storage systems and addresses the challenges of high-speed spin tests in vacuum environments. By implementing a small stiffness pivot-jewel bearing and a spring squeeze film damper, these researchers designed a cost-effective, long-lasting spin system, achieving stable operation at 50,000 rpm with the theoretical results aligning with experimental findings. In another study [33], due to the limited data on the performance of burst containments for high-speed rotating machines, there was a need for low-cost test methods to develop optimized containment structures. Consequently, a low-cost test rig was designed to systematically investigate the performance of different containment structures and materials, with the collected data and subsequent analyses enabling the assessment of the effectiveness of various burst containments.

This paper focused on examining the rotor dynamic effects for the spin test rig in detail. First, a Discrete Model (henceforth DM) of the system was established in the Matlab/Simulink environment to develop a preliminary design of the drive shaft, which rotates the test specimens. Then, both two- and three-dimensional modal and harmonic response analysis were carried out using the finite element approach to verify numerical results obtained from DM studies. These numerical results were validated with the Hummer test, and it was observed that the maximum error percentage was as small as 4.85. Bearing stiffness values were selected considering the loads in the supports due to permissible unbalance, and thus, non-linear rotor dynamic effects were also included in the calculations. It was also assumed that there was no axis misalignment in the system, and inspections were carried out only for the first engine order. Additionally, since the system is tested under vacuum, there is no aerodynamic damping. In this context, it is only possible to talk about damping of the system. This damping ratio is below 3% and is considered to be negligible in the calculation of the natural frequency. This system damping was used as input data in alternating stress calculations, and an HCF evaluation was made.

This study, unlike examples found in the literature, presents a preliminary design for rotordynamics using a discrete model. In this way, the bearing support regions are optimally determined based on the results obtained from DM, which is the first step in the overall system design. Furthermore, instead of assuming constant bearing stiffness values, our study incorporates nonlinearity based on the unbalance force. By selecting bearing stiffnesses depending on the load rather than using constant values in rotordynamic calculations, more accurate computational results consistent with the hummer test can be achieved. As mentioned, the first stage of our study is to build a DM in Matlab Simulink and to calculate the natural frequencies of the system. Following this, a general axisymmetric finite element model was established, and the accuracy of the results obtained from DM was examined in detail using a two-dimensional approach. While the results obtained from DM and the general axisymmetric finite element model are consistent, a three-dimensional finite element model was also created to consider the geometry deviating from axial symmetry and to perform harmonic response analysis. The aim of two-dimensional analysis is the fast verification of DM results because of the low mesh element number. However, harmonic response and related alternating stresses cannot be calculated with this axisymmetric two-dimensional model. As a consequence of this a three-dimensional model was needed. In spin test systems, since the test specimen is tested under vacuum, the absence of aerodynamic damping is assumed, and the damping ratio corresponding to the relevant mode obtained from impact tests has been directly

used as input data. The harmonic force generated from the unbalance was given as input data to the 3D finite element model to find the system response. By performing detailed rotordynamic calculations, the test specimen can be brought to the desired rotational speeds while avoiding vibration effects, thus preventing damage to the drive shaft and related components.

2. Materials and Methods

In this paper, applications for the most appropriate design of the spin test rig, which will not be affected by alternating stresses due to vibration, are presented. The primary objective of this study is to present solutions that minimize vibration effects caused by rotordynamics during the testing of high-speed components, such as those in spin test systems. In this context, the aim is to establish an optimal rotordynamic layout during the preliminary design phase by developing a discrete model in Matlab Simulink that incorporates factors influencing the vibration characteristics. By developing a discrete model based on the equations of motion, the rotordynamic characteristics of high-speed rotating components can be determined during the preliminary design phase. This approach allows for the potential vibration issues that may arise during the detailed design phase to be addressed and mitigated at the preliminary design stage. In this context, a discrete rotor dynamics model was established in MATLAB SIMULINK. The results obtained from this model were compared with those from general axisymmetric and 3D modal analyses. Input data used for calculations, including angular speed, bearing stiffness, and damping ratio, were incorporated into the harmonic analysis. Bearing stiffness values were not treated as constants; instead, nonlinear stiffness behaviors were used in both axial and radial directions. The damping ratio applied in this study was obtained directly from impact tests on the relevant mode. The advantage of conducting tests under vacuum is that aerodynamic damping effects are eliminated, allowing for the direct use of system damping data. Results from both the finite element approach and the 3D MATLAB SIMULINK rotordynamics model were compared with test data. Error rates resulting from these comparisons are presented in the results section. The algorithm for this study is illustrated in Figure 1. To enhance the accuracy of this study, calculations and impact tests were conducted on two distinct test specimens with different moments of inertia and masses. The first test specimen weighs 10 kg, while the second specimen weighs 4 kg. The vacuum chamber in which the tests were conducted is shown in Figure 2, and the details of the test specimens and shaft connections are provided in Figure 3.

The primary purpose of using the two-dimensional analysis model is to keep the number of mesh elements at a minimum, enabling fast solution time and facilitating the comparison of preliminary Simulink results. However, in two-dimensional analyses, the effects of sections that break axial symmetry on modal analyses are neglected. Therefore, the Simulink results, which are initially validated through two-dimensional analyses, are further verified in the next phase using three-dimensional models. The model created in the Simulink environment is highly effective in determining the bearing stiffness and axial locations. This allows for a rapid execution of rotordynamic layout studies using the discrete model in Simulink. Moreover, the bearing locations and stiffness values can be parametrized within the model to derive the optimal rotordynamic layout. In these studies, the preliminary validations are performed using two-dimensional analyses, assuming axial symmetry. Subsequently, three-dimensional analyses are conducted to account for the effects of sections that disrupt axial symmetry, incorporating them into the rotordynamic calculations.

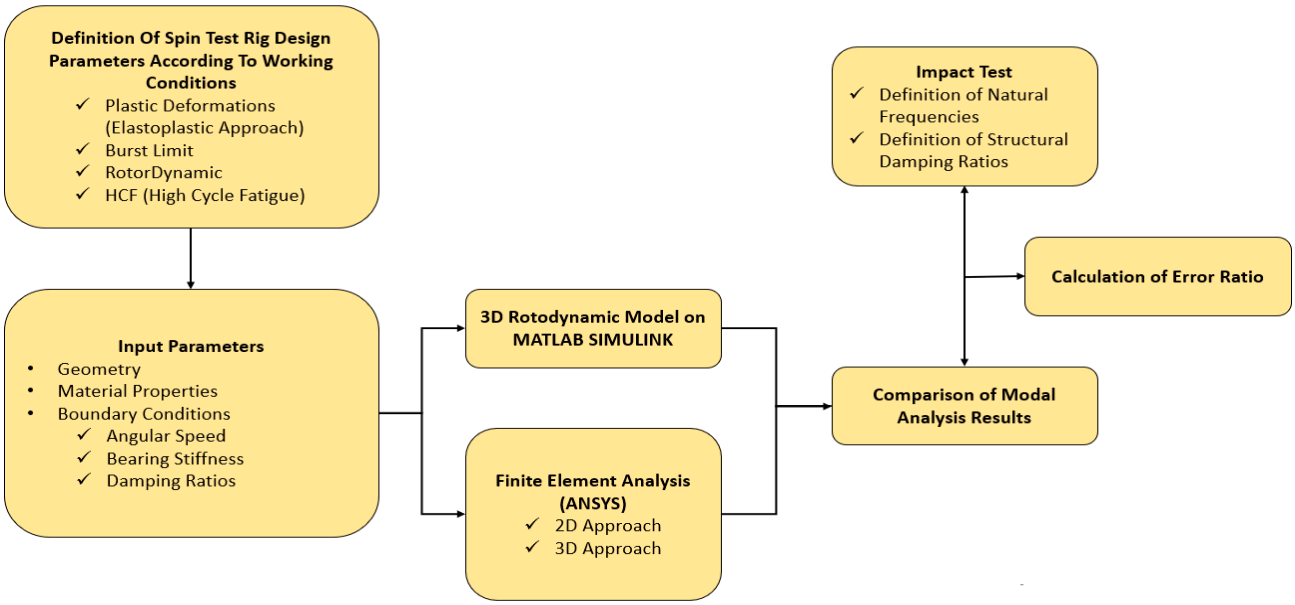


Figure 1. Algorithm of this study.

The spin test system consists of three main components: the power transmission system, rotor rig, and vacuumed cabin, as seen in Figure 2. The system specifications are as follows: For the Inconel 718 material used in the test rotor, the maximum temperature is 700 °C. The maximum rotational speed for the test rotor is 60,000 rpm. The vacuum level should be equal to or less than 50 Pa. The geometric dimensions of the main rotor shaft and bearing positions have been determined through an optimization study. The test rig and the main rotor shaft will be connected through bolt fastening, allowing for the testing of discs with different geometries.

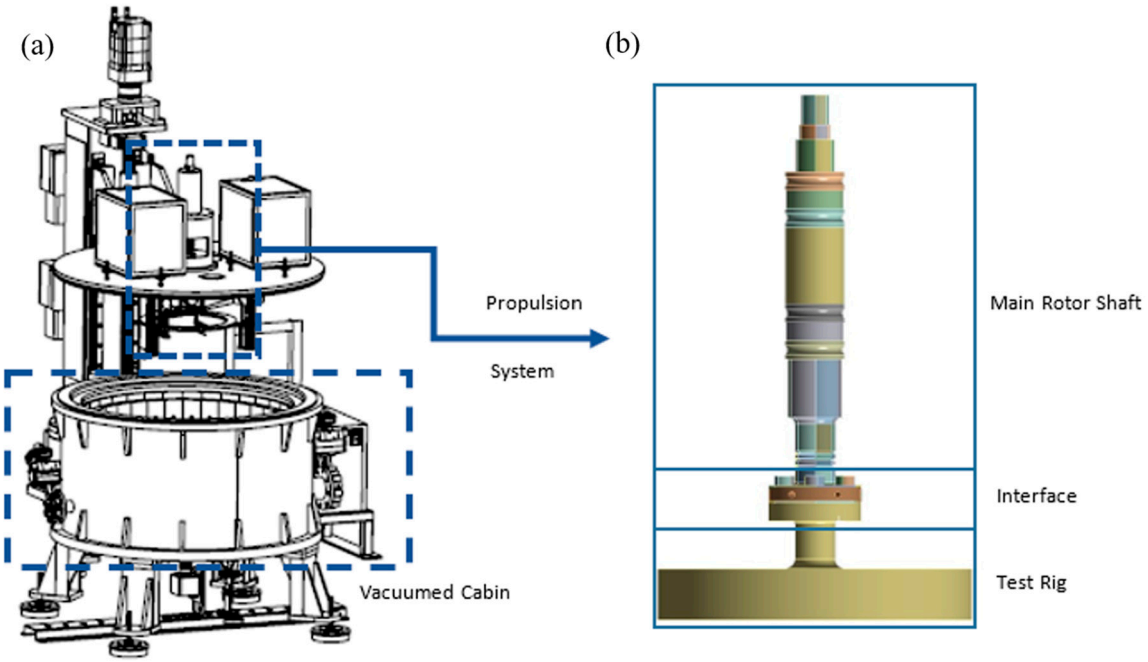


Figure 2. Definition of the system (**a**) spin test rig (**b**) assembly of shaft.

The test specimens and the drive shaft to which they are connected in the spin test rig are presented in detail in Figure 3. The first specimen weighs 10 kg and will be tested at 30,000 RPM, while the other specimen weighs 4 kg and will be tested at 60,000 RPM.

Rotordynamic calculations have been performed separately for each of these specimens. Boundary condition definitions for the drive shaft at the inner race of the bearing have also been provided in detail.

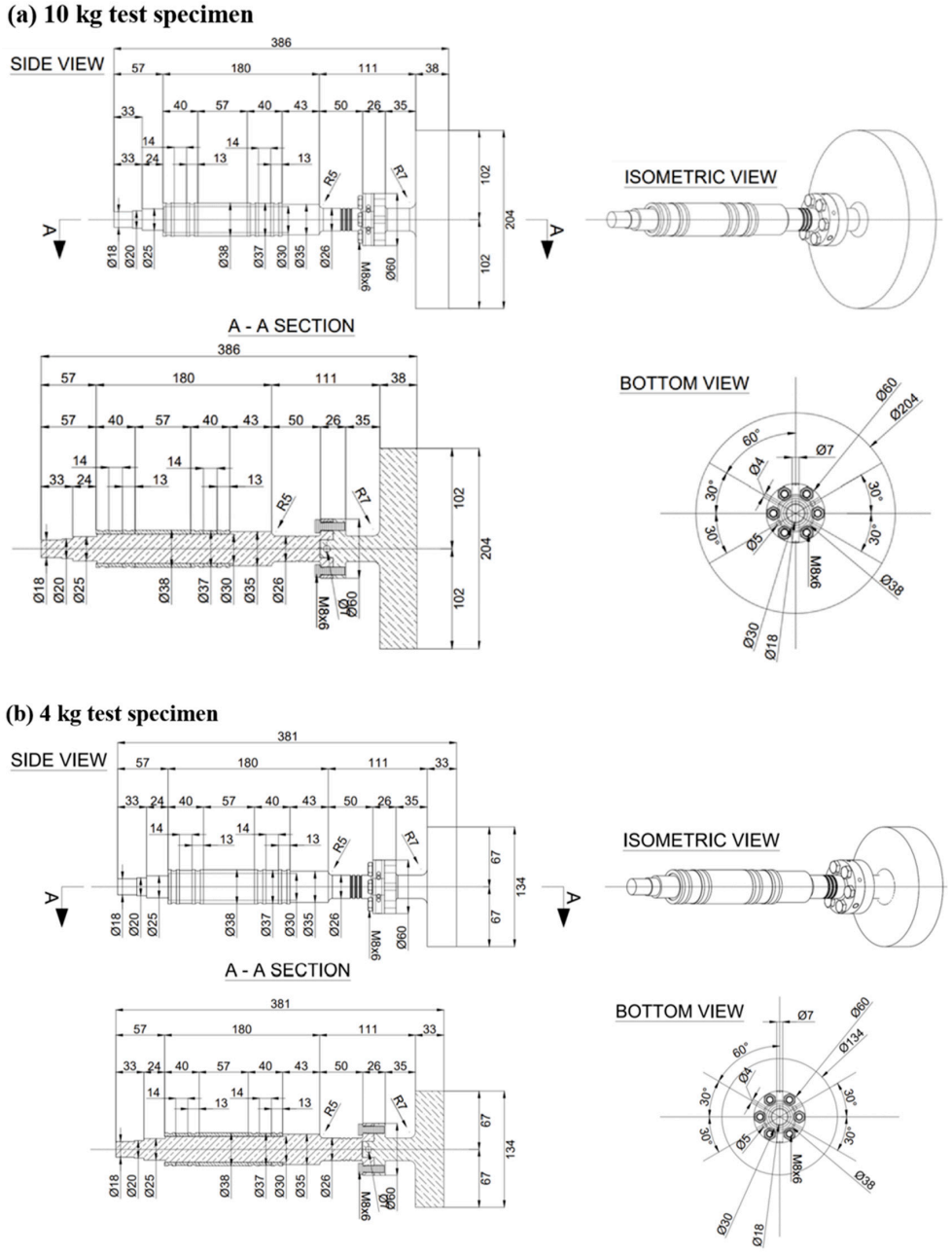


Figure 3. Diameters of Test Specimen (**a**) 4 kg specimen drawings (**b**) 10 kg specimen drawings.

The DM of the shaft represents a flexible body as a combination of a rigid-body model and a deformation model. The rigid-body model accounts for the body's rotation and translation movements without any deformation. This model calculates shape changes at specific points on the body, which are derived using the rigid-body model. Achieving accurate results with this method relies on the spatial distribution of the geometry's mass, inertia, stiffness, and damping properties. The DM divides the body into a mesh consisting of numerous nodes, each with six degrees of freedom. The details of the DM are depicted in Figure 4.

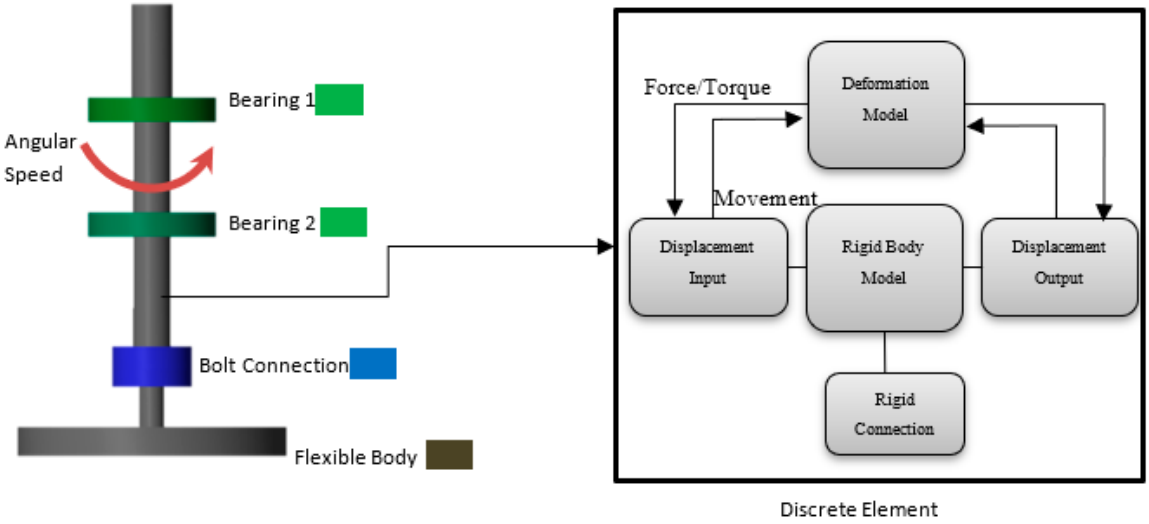


Figure 4. Discrete model of the shaft.

In the mathematical model of the spin shaft, the main rotor shaft is modeled as flexible. Using the developed model, it is also possible to size the rotor shaft under relevant constraints with optimal values. Figure 4 illustrates the main rotor shaft and its bearings. For a shaft supported by bearings at two points and free at one end, the translational and rotational movements of the center of mass along two different axes are defined as follows:

The mathematical model of the spin shaft supported by bearings in two regions is presented in Figure 5. Based on this mathematical approach, the 3D rotordynamics model developed in the MATLAB Simulink is detailed in Figure 4.

$$x_{rs,G} = \frac{(a+b)x_2 - bx_1}{a} \tag{1}$$

$$y_{rs,G} = \frac{(a+b)y_2 - by_1}{a} \tag{2}$$

$$\theta_{x,G} = \frac{x_1 - x_2}{a+b} \tag{3}$$

$$\theta_{y,G} = \frac{y_1 - y_2}{a+b} \tag{4}$$

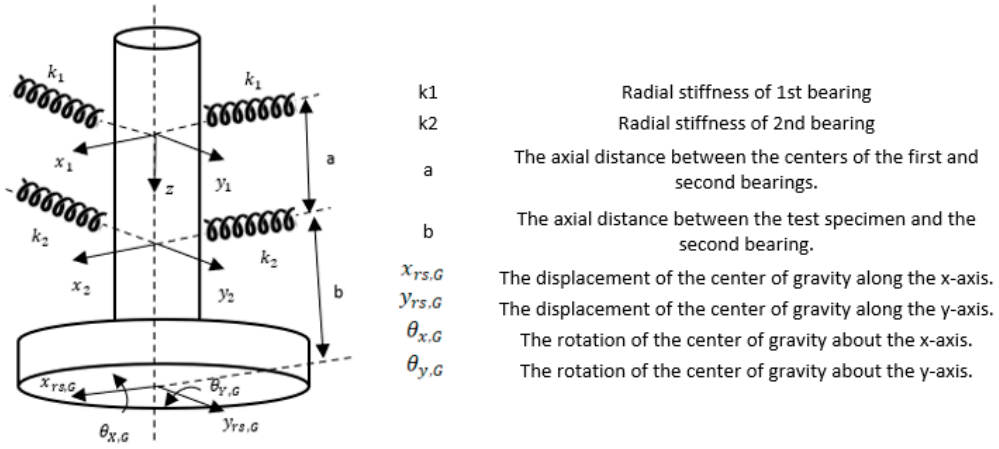


Figure 5. Mathematical model of spin shaft.

Based on this, the equations of motion are derived using the Euler-Newton method as follows:

$$m_{rs}\ddot{x}_{rs,G} + (k_1 + k_2)x_{rs,G} + (k_1(a+b) + k_2 b)\theta_{y,G} = F_{rs,x} \tag{5}$$

$$m_{rs}\ddot{y}_{rs,G} + (k_1 + k_2)y_{rs,G} + (k_1(a+b) + k_2 b)\theta_{x,G} = F_{rs,y} \tag{6}$$

$$J_{T,rs}\ddot{\theta}_{x,G} + J_{P,rs}\Omega\dot{\theta}_{y,G} + (k_1(a+b) + k_2 b)x_{rs,G} + \left(k_1(a+b)^2 + k_2 b^2\right)\theta_{x,G} = M_{rs,x} \tag{7}$$

$$J_{T,rs}\ddot{\theta}_{y,G} - J_{P,rs}\Omega\dot{\theta}_{x,G} - (k_1(a+b) + k_2 b)y_{rs,G} + \left(k_1(a+b)^2 + k_2 b^2\right)\theta_{y,G} = M_{rs,y} \tag{8}$$

Here, $J_{T,rs}$ is the transverse mass moment of inertia and $J_{P,rs}$ is the polar mass moment of inertia, and they are defined by the following expressions.

$$J_{T,rs} = \frac{m_{rs}}{4}\left(R_{rs}^2 + \frac{1}{3}L^2\right), \quad J_{p,rs} = \frac{m_{rs}R_{rs}^2}{2} \tag{9}$$

The system matrices in the equation of motion consist of the global mass matrix $\underbrace{M}$, the global gyroscopic matrix $\underbrace{G}$, and the global stiffness matrix $\underbrace{K}$ as shown in Equation (1). The generalized external force vector for the global system, denoted by $\underbrace{F}$, encompasses all external disturbance forces and torques that affect the dynamics of the global system. All system matrices and vectors are organized in the same sequence as the nodal displacements in vector $\underbrace{q}$ as seen in Equation (2).

$$\underbrace{M}\,\underbrace{\ddot{q}} + \underbrace{G}\,\underbrace{\dot{q}} + \underbrace{K}\,\underbrace{q} = \underbrace{F} \tag{10}$$

$$\underbrace{q} = \begin{bmatrix} q_1 & q_2 & q_3 & \cdots & q_{n+1} \end{bmatrix}^T \tag{11}$$

In the rotor dynamics studies, bearing stiffness values were not treated as constants in either the radial or axial directions; instead, the stiffness characteristics obtained from tests were utilized as input data. The nonlinear stiffness behavior curves for both radial and axial directions are presented in Figure 6. When applying bearing stiffness values in rotor dynamics calculations, the selection was based on the allowable unbalance load for radial stiffness, while mounting loads were considered for axial stiffness. This approach incorporates the nonlinear stiffness effects of the bearings into the calculations. As a result, the rotor dynamics calculations yield results that are more consistent with the experimental data.

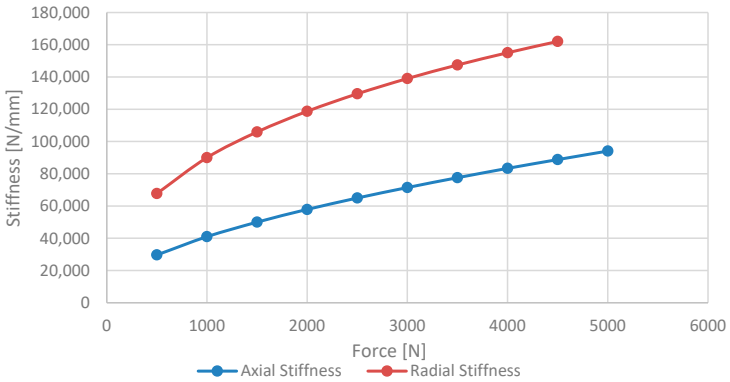


Figure 6. Axial and radial stiffness of bearing.

The system used for measuring radial and axial stiffness of bearings is detailed in Figure 7. The system includes a 3-axis accelerometer and a thermocouple. The bearings' stiffness, characterized by nonlinear properties, is determined based on elastic displacement

values obtained from different radial and axial loading conditions. The accuracy of these measurements is crucial, requiring minimal error for the successful completion of the application. Therefore, laser displacement sensors have been utilized for the measurements.

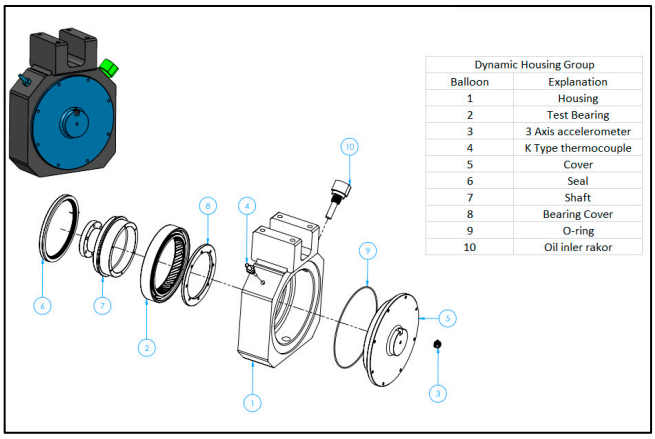


Figure 7. Bearing Stiffness Test Rig.

Finite element analyses of the spin test rig shaft were conducted using both general axisymmetric and 3D approaches. General axisymmetric mesh elements were employed in the general axisymmetric rotordynamics calculations. The mesh element selected was Solid 272, with the number of nodal planes set at 12. The primary advantage of using general axisymmetric rotordynamics analyses is the significantly faster computation compared to three-dimensional analysis. In the section of Results, the detailed information on the mesh number, natural frequencies, and solution times relative to the number of nodal planes will be given. In the general axisymmetric rotordynamics calculations, bolt head elements were modeled using point mass elements, allowing for the effective mass to be incorporated into the system within the general axisymmetric analysis framework. Differences between the 3D and general axisymmetric analysis mass matrices can lead to variations in the calculated natural frequencies. The use of point mass elements helps to mitigate discrepancies between the mass matrix and moment of inertia in both general axisymmetric and 3D analyses. Two-dimensional and three-dimensional finite element rotordynamics analysis models are illustrated in Figure 8.

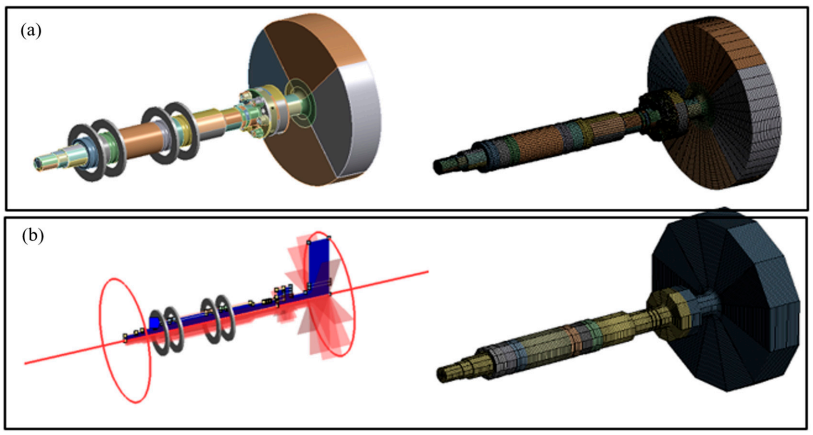


Figure 8. Finite element model of system (**a**) 3D FEM model (**b**) 2D FEM model.

3D analyses were utilized for both stress distribution and alternating stress calculations in the rotating components of the shaft assembly. The primary goal of employing 3D analysis was to accurately capture stress distribution in non-axisymmetric regions with a high degree of convergence. The 3D analysis model, which facilitated these stress

calculations, is depicted in Figure 9, with the mesh properties of the finite element model detailed in Table 1. In contrast, 2D analyses would exhibit significant error rates in non-axisymmetric areas, thus necessitating the use of 3D models for precise stress calculations. Modal analyses, however, were conducted more efficiently using general axisymmetric models in 2D, which allowed for rapid computation of stiffness and mass matrices. This approach enabled the swift execution of parametric modal analyses, with results compared against other simulations and experimental data.

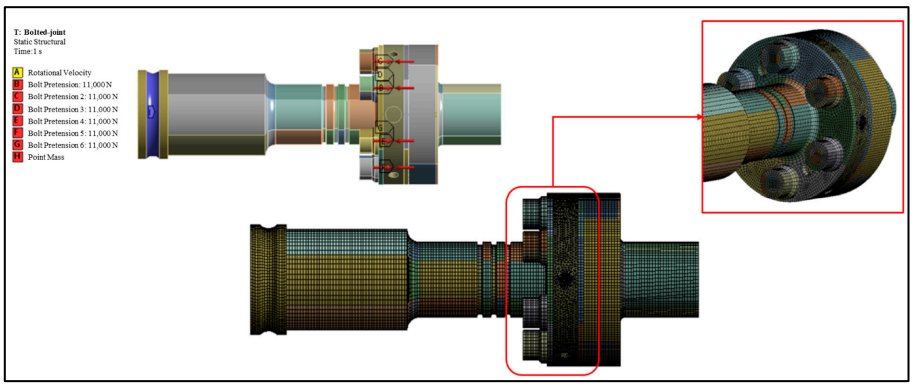


Figure 9. 3D Finite element model for stress calculations with solid 186 mesh element.

Table 1. Mesh properties of 3D stress model.

Element Type	Solid 186
Element Number	420,022
Node Number	1,300,804
Averaged Aspect Ratio	1.7672
Averaged Element Quality	0.85226

As part of this study, an impact test was employed for the validation of the DM and finite element models. An accelerometer (Bruel & Kjaer Type 4514) is affixed to the rotor disc, and impacts are imparted using a modal hammer (Bruel & Kjaer Type 8206-003) at distinct locations on the rotor disc to effectively average out experimental noise. Subsequently, these signals are transmitted to a laptop via an ADC (Bruel & Kjaer PC Card Front End 3560-L) for the computation of frequency response functions (FRFs). The relevant test setup is shown in Figure 10.

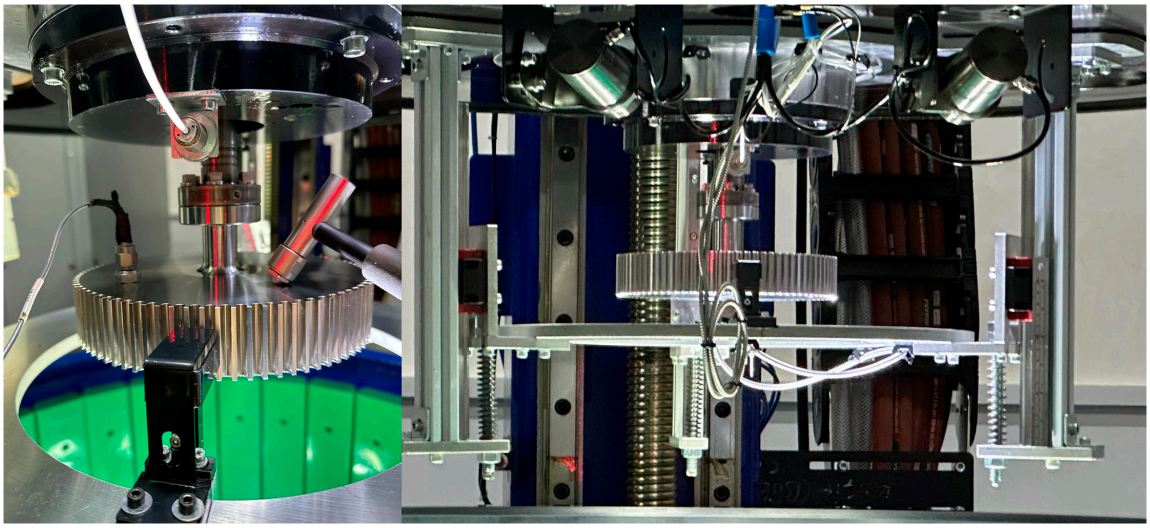


Figure 10. Experimental test set-up.

The material properties of the shaft and the test rig are listed in Table 2. Based on rotordynamics calculations, when performing alternating stress evaluations, it is essential to prevent plastic deformation on the drive group and shaft components within the system. In this context, only the part forced to the burst limit should be examined for crack and fracture conditions. This can be carried out depending on the test requirements. The stress obtained by adding the alternating stress values from the harmonic analyses to the operating conditions should not exceed the yield limit in the drive group. The elastic limits of the materials used are provided in Table 2.

Table 2. Material properties of Inconel 718 and 4340 steel.

Material Properties	Inconel 718	4340 Steel
Density	8240 kg/m^3	7850 kg/m^3
Young's Modulus	203.6 GPa	200 GPa
Poisson Ratio	0.29 [−]	0.3 [−]
Yield Strength	1018.9 MPa	470 MPa
Ultimate Strength	1275.8 MPa	745 MPa

3. Results

In this section of this study, the results from finite element analysis, Simulink, and impact tests are presented. The finite element analysis results are provided for both general axisymmetric (in other words, the 2D model) and 3D approaches. Detailed comparisons of these results are shown in Table 3 for the 10 kg test specimen. Additionally, the results from the finite element modal analysis, conducted using the general axisymmetric approach with varying numbers of node planes, are presented in Table 4. The modal analysis identified natural frequencies at 234 Hz and 528 Hz for the 10 kg test specimen. These frequency values were obtained from both the general axisymmetric and 3D modal analyses. Additionally, for the 10 kg test specimen, the maximum discrepancy between the finite element analysis results and the Simulink results was found to be 4.2% at the first natural frequency of 232 Hz. The difference was calculated to be 0.73% in the 532 Hz region, where the second natural frequency occurs. The general axisymmetric and 3D analysis results are illustrated in Figure 11.

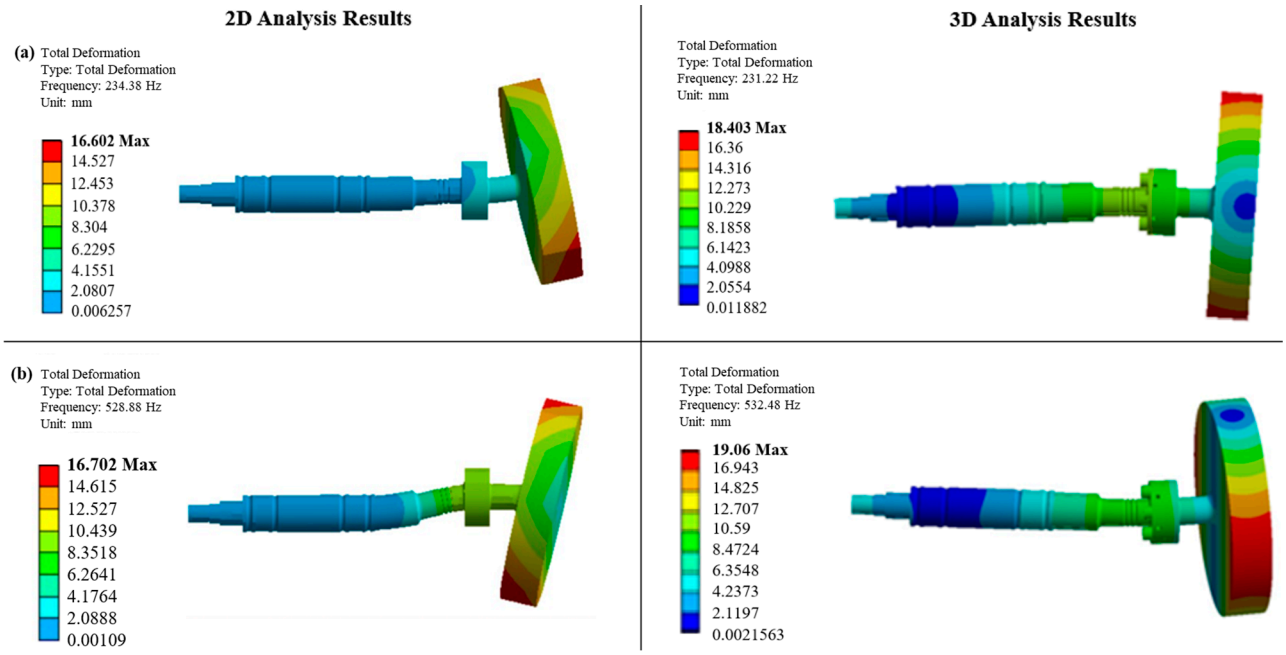


Figure 11. General Axisymmetric and 3D modal analysis results (**a**) 1st natural frequency (**b**) 2nd natural frequency.

Table 3. Modal analysis and test results for 10 kg test specimen.

Analysis Type	1st Natural Frequency	2nd Natural Frequency	Relative Error Percentage with Respect to Impact Test Result for 1st Natural Frequency	Relative Error Percentage with Respect to Impact Test Result for 2nd Natural Frequency
General axisymmetric	234.38 Hz	528.88 Hz	0.96%	1.68%
3D	231.22 Hz	532.48 Hz	0.39%	2.37%
Simulink	241.9 Hz	528.6 Hz	4.2%	1.63%
Impact Test	232.14 Hz	520.13 Hz	-	-

Table 4. General axisymmetric modal analysis results depend on the number of nodal planes.

General Axisymmetric Nodal Plane Number	Element Number	Node Number	1st Natural Frequency	2nd Natural Frequency	Solution Time
6	4259	78,520	234.38 Hz	528.88 Hz	46 s
8	4259	104,536	234.38 Hz	528.88 Hz	1 m 29 s
10	4259	130,552	234.38 Hz	528.88 Hz	2 m 47 s
12	4259	156,568	234.38 Hz	528.88 Hz	4 m 57 s

Mesh sensitivity analyses were conducted for the general axisymmetric analyses, and the mesh element size was parameterized. In this context, the results of the mesh sensitivity analyses for the model corresponding to the 4 kg test data are detailed in Table 5. According to the obtained results, applying an element size of 2 mm is quite sufficient. The mesh structure created in modal analyses directly forms the stiffness and mass matrices. Therefore, when the mesh size is below a certain element size, the variation in natural frequencies becomes nearly zero.

Moreover, after determining the appropriate mesh element size as 1 mm, a solution was performed based on the number of nodal planes for the solid 272 mesh element, and the corresponding results are presented in Table 4.

Mesh sensitivity studies conducted for the 4 kg test specimen are detailed in Figure 12, and the analysis results based on mesh element size are presented in Table 5. The studies indicate that even with a 2 mm mesh element size, the maximum frequency deviation remains below 0.8%. This suggests that the mesh element sizes applied for the modal analysis are appropriate.

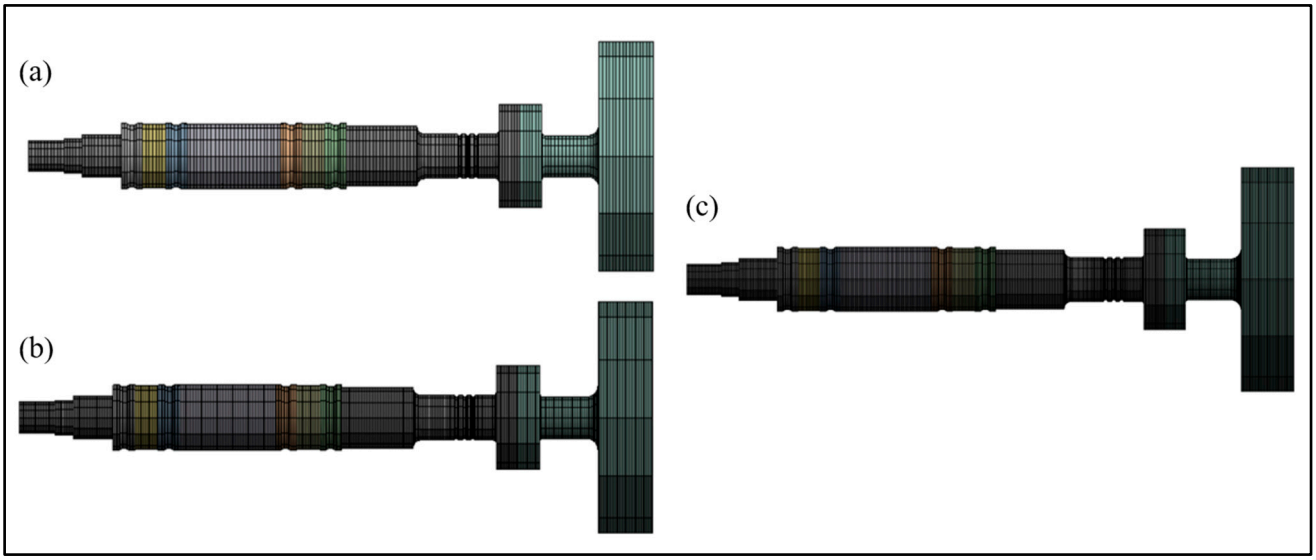


Figure 12. Different mesh size of spin shaft model (**a**) 2 mm element size (**b**) 1 mm element size (**c**) 0.5 mm element size.

The defined material properties were used as input data for the analysis model. Contact loads arising from interference fit, bolt pretensions, and angular velocity were applied as boundary conditions for the 3D structural simulations. The Von Mises stress distribution for the shaft is shown in Figure 13 for a 10 kg test specimen. Based on the stress distribution, the maximum equivalent stress was calculated to be 374.39 MPa. This value is below the yield limit, indicating that no plastic deformation is expected to occur in the shaft.

Table 5. Natural frequencies according to mesh element size for general axisymmetric analysis [4 kg test specimen].

General Axisymmetric Mesh Element Size [mm]	Element Number	Node Number	1st Natural Frequency	2nd Natural Frequency	3rd Natural Frequency	Solution Time
0.5	31,011	374,760	239.32 Hz	446.41 Hz	641.62 Hz	1 h 30 m
1	7688	93,714	240.08 Hz	447 Hz	643.27 Hz	15 m 6 s
2	2016	24,948	241.08 Hz	448.48 Hz	646.79 Hz	2 m 12 s

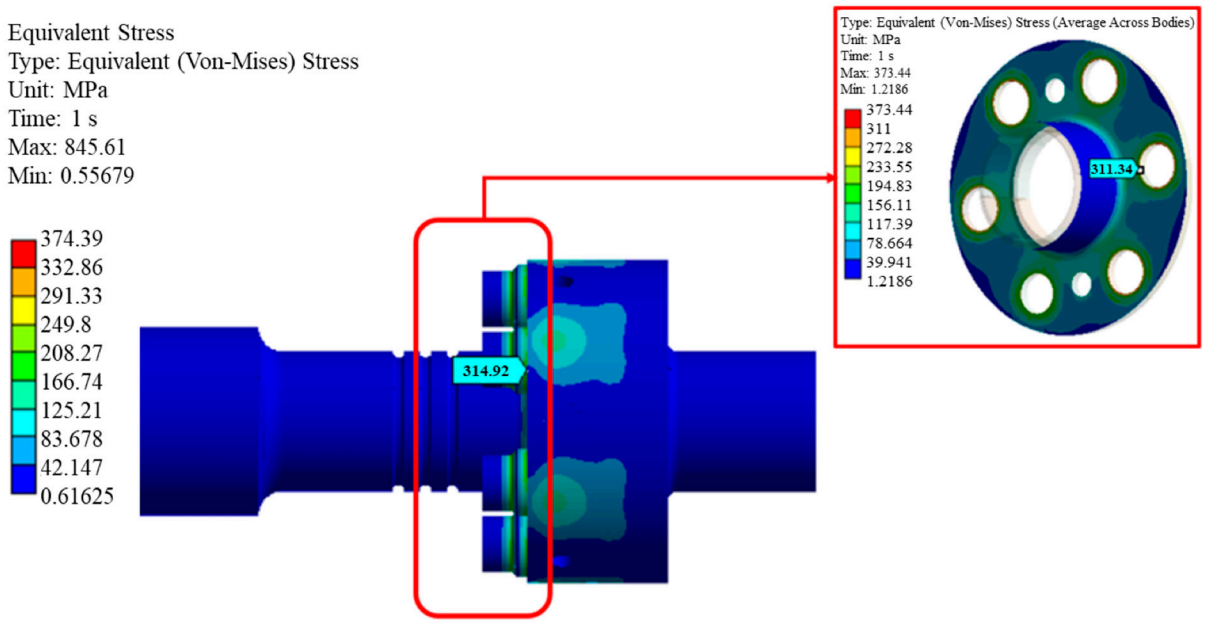


Figure 13. Stress distribution of 3D analysis model.

The stress distribution calculated from the structural analysis, using 31,920 rpm (equivalent to 532 Hz) as input data for a 10 kg test specimen, is shown in Figure 13. However, the alternating stresses resulting from the critical speed that would occur if the shaft operated at 532 Hz were calculated using harmonic analysis. When applying a damping coefficient of 0.5%, as determined from local impact tests, the maximum alternating stress is found to be 64.87 MPa. In contrast, applying a damping ratio of 2.8%, obtained from the hammer test conducted on the assembly, results in a maximum alternating stress of 11.54 MPa. Both the maximum equivalent stress from the structural analysis and the maximum alternating stress from the harmonic analysis affect the same section of the shaft. Therefore, a high cycle fatigue evaluation was performed for this region, and the material yield limit was not exceeded even when the lowest damping ratio was applied.

Alternating stress evaluation was conducted based on the damping ratios for the region where the maximum equivalent stress (Von Mises Stress) was calculated. The stress distribution and the alternating stress graph obtained from the 3D harmonic analysis are presented in Figure 14 for a 10 kg test specimen. The alternating stress graphs, generated using damping ratios of 0.5% and 2.8% in the harmonic analysis, are shown in Figure 15. In

these calculations, the force applied to the rotor, which underwent a G6.3 balancing process according to the standard [34], was determined to be 404 N.

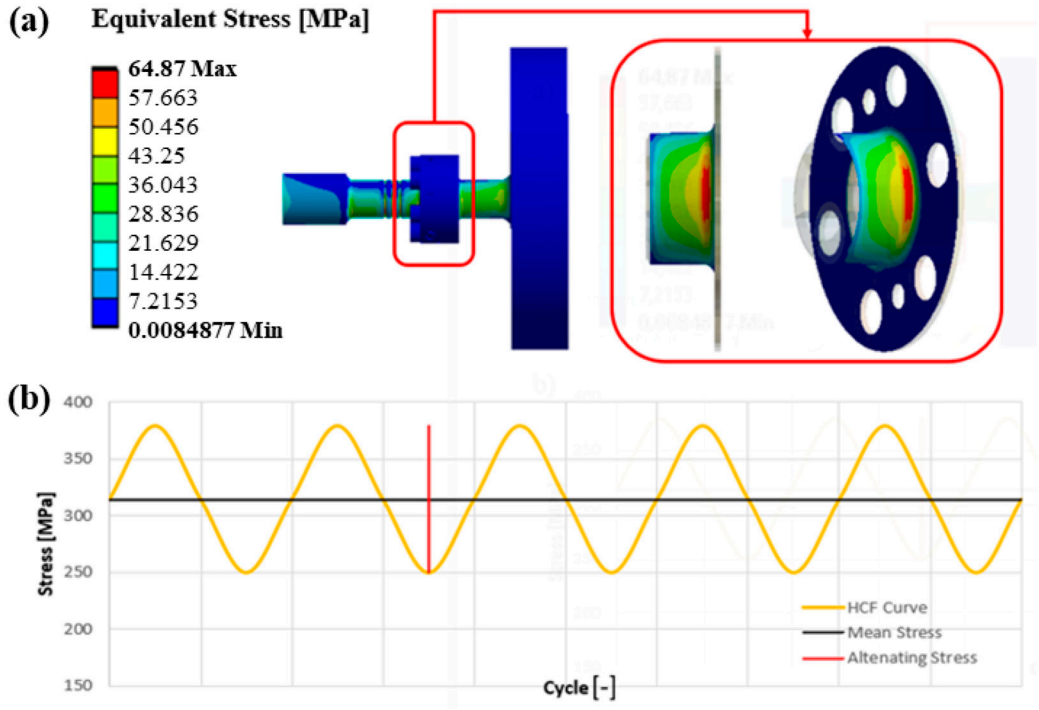


Figure 14. 3D harmonic analysis results (**a**) Stress distribution of model (**b**) Alternating stress curve.

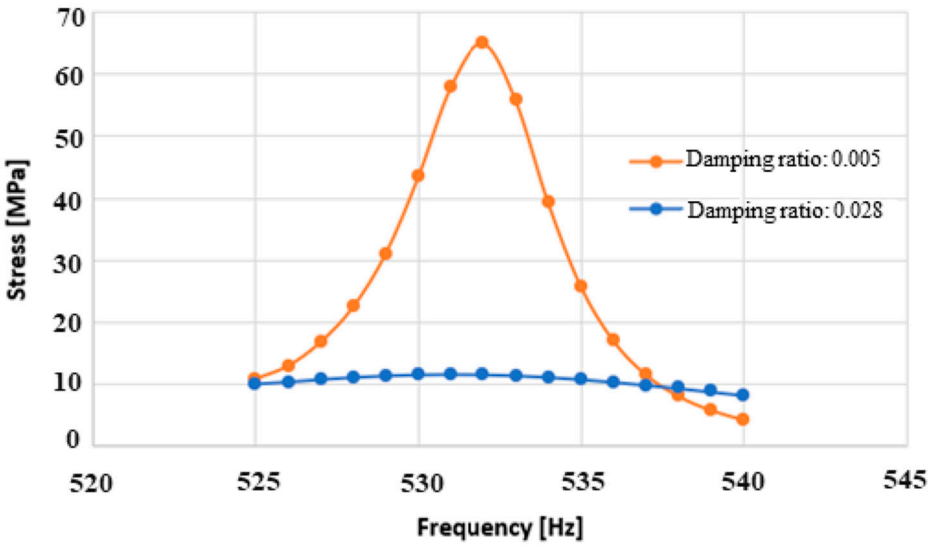


Figure 15. Alternating stress according to frequency with different damping ratios.

Based on the layout created according to the Matlab Simulink model, finite element and testing studies were also carried out for a test specimen with a mass of 4 kg. Along with these studies, the accuracy of the model created in the Simulink environment was also compared with another test data. The finite element studies of the 4 kg test specimen were performed using both the general axisymmetric approach and the three-dimensional approach, similar to the 10 kg test specimen. The connection details for the 4 kg test specimen and the drive shaft are presented in Figure 16.

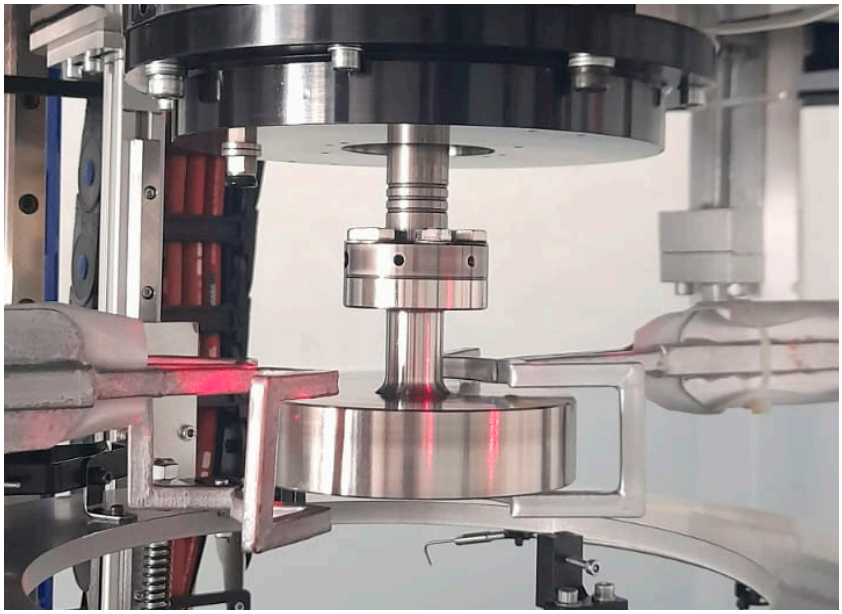


Figure 16. 4 Kg test specimen with drive shaft.

The mode shapes obtained from the two- and three-dimensional modal analysis results for the 4 kg test specimen are presented in Figure 17. The mode identified at 448 Hz is a torsional mode, while the mode detected at 635 Hz can be classified as a bending mode.

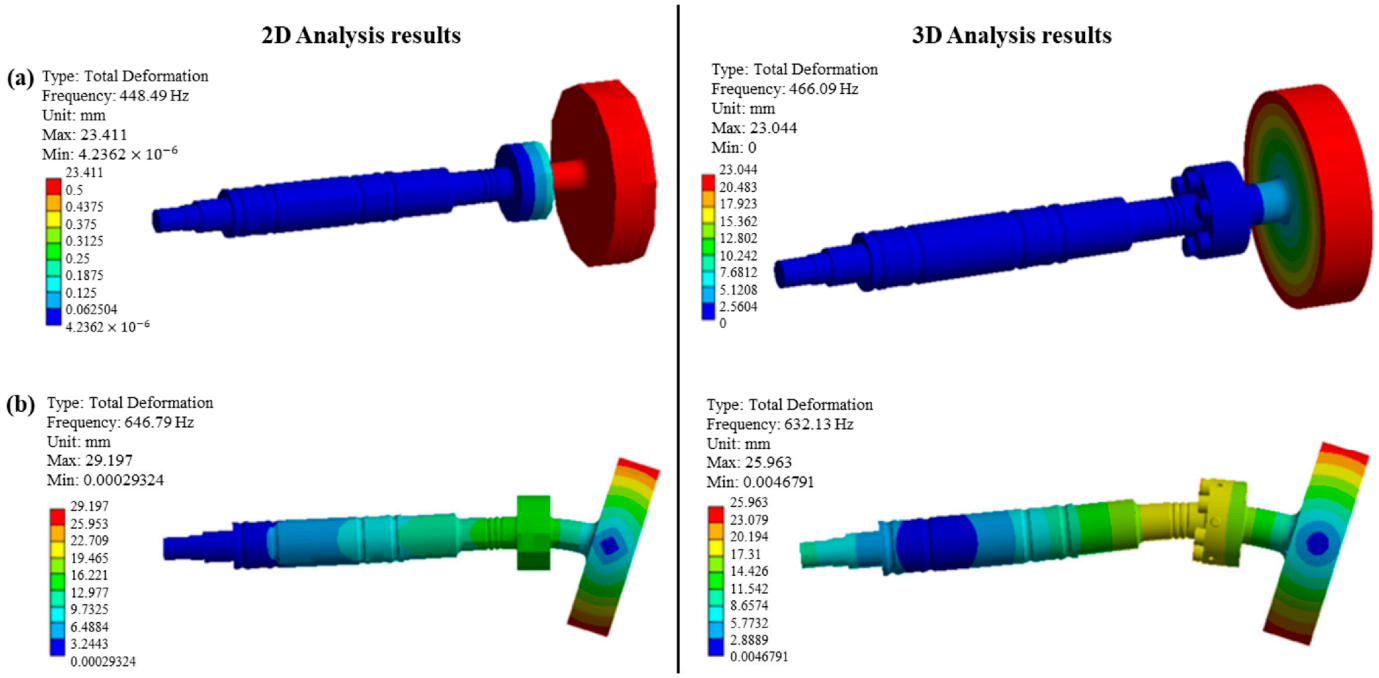


Figure 17. 4 kg test results (**a**) Torsional mode (**b**) Bending mode.

The first three natural frequencies of the 4 kg test specimen were calculated using the Simulink tool developed for the preliminary design phase. Subsequently, the preliminary design was verified through both general axisymmetric approaches and three-dimensional modal analyses, followed by impact tests. The error rates observed in the natural frequencies based on all these results and impact tests are detailed in Table 6.

Table 6. Modal analysis and test results for 4 kg test specimen.

Analysis Type	1st Natural Frequency [Hz]	2nd Natural Frequency [Hz]	3rd Natural Frequency [Hz]	Relative Error Percentage with Respect to Impact Test Result for 1st Natural Frequency [−]	Relative Error Percentage with Respect to Impact Test Result for 2nd Natural Frequency [−}	Relative Error Percentage with Respect to Impact Test Result for 3rd Natural Frequency [−]
General axisymmetric	241.08	448.49	646.79	−5.49%	0.27%	1.86%
3D	262.44	466.09	632.13	2.88%	4.2%	−0.45%
Simulink	268.12	439.96	665.14	4.85%	−1.64%	4.75%
Impact Test	255.1	447.3	635	-	-	-

For the 4 kg test specimen, the equivalent stress distribution obtained from the structural analysis conducted at the 60,000 rpm boundary condition is presented in Figure 18. The strain distribution for the relevant region was also verified in the finite element model, and detailed mesh sensitivity analyses were performed, with converged stress results provided.

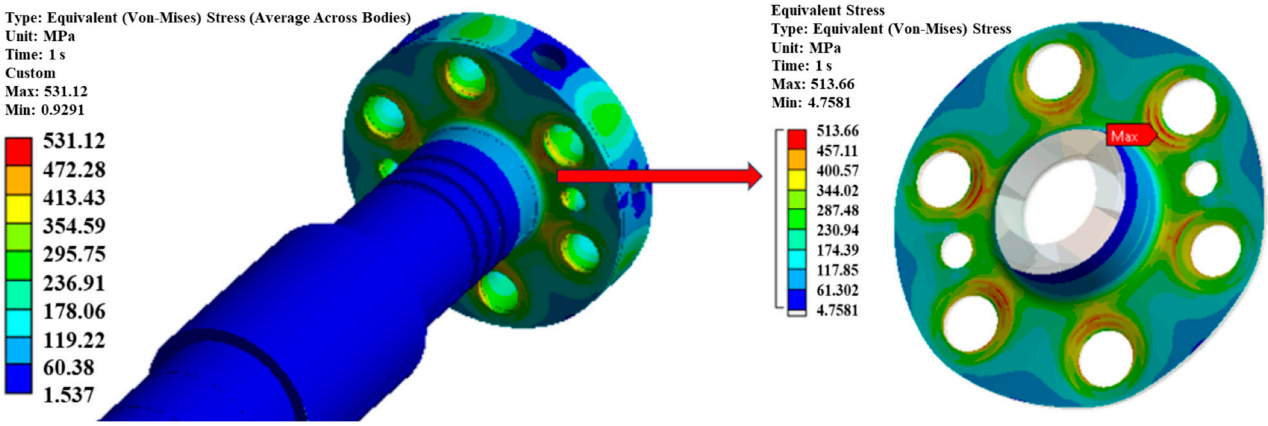


Figure 18. Equivalent stress distribution for shaft for 4 kg test specimen under 60,000 rpm.

4. Discussion

In spin test rigs, plastic deformation, crack propagation, and burst phenomena can occur on the test specimen. For accurate results, tests must be conducted without external influences such as imbalance, vibration, and misalignment. A critical speed should not exist within ±20% of the test speed. Vibrations can lead to inaccurate results by affecting stress variations, potentially causing High Cycle Fatigue (HCF) and resulting in damage to the test specimen and associated components. It is crucial to ensure that the test component is operated without exposure to vibrations. Detailed rotor dynamics calculations are essential to ensure test accuracy and design reliability, especially in high-speed systems where bearing stiffness must be modeled nonlinearly in both axial and radial directions. Radial stiffness should be based on allowable imbalance forces, while axial stiffness should account for assembly loads to create an accurate mathematical model incorporating nonlinear bearing stiffness. Performing spin tests under vacuum removes aerodynamic damping, allowing the direct use of hammer test-derived damping ratios in alternating stress calculations. Since damping values from hammer tests are below 3%, their effect on natural frequencies is negligible. However, systems with squeeze film dampers (SFD) and aerodynamic damping require consideration of damping-related critical speeds and appropriate coefficients in harmonic response calculations.

In this study, a discrete model approach was applied to the equations of motion, utilizing a rotordynamic tool established in MATLAB Simulink to achieve the rotordynamic layout during the preliminary design phase. Furthermore, in the created model, bearing

stiffness values were not assumed to be constant; instead, radial stiffness values based on unbalance forces and axial stiffness values based on assembly loads were integrated into the system. To validate the accuracy of this study, tests were conducted on two different specimens weighing 10 kg and 4 kg, respectively. For the 10 kg test specimen, the maximum natural frequency deviation between the results and the Simulink-based rotordynamic calculations was found to be 4.2%. A similar approach was applied to the 4 kg test specimen, with the maximum frequency deviation calculated as 4.85%. The primary factors contributing to the discrepancies between the test results and Simulink outcomes include contact damping, Multi-Point Constraint (MPC) connection assumptions, and differences in mass and inertia tensor that disrupt axial symmetry.

In this study, it was observed that the damping ratio of the rotating assembly was higher than that of individual components due to new natural frequencies and contact damping. Damping ratio increased from 0.5% in individual tests to 2.8% after assembly. Both assembly and shaft-only damping ratios were calculated for alternating stress. The resulting stress curve showed that the shaft's critical region remained below the yield point. The SIMULINK model, using a discrete rotor dynamics approach, showed a 4.2% error for the first natural frequency and a 1.63% error for the second, compared to finite element calculations, facilitating quicker bearing location identification and geometric optimization for a 10 kg test specimen.

Similar studies were also conducted for the 4 kg test specimen. The rotordynamic layout for the part to be tested at higher speeds compared to the 10 kg specimen has been completed. Calculations using a damping ratio of approximately 3% resulted in low alternating stress values, and the yield limit of the drive shaft within the system was not exceeded. For both specimens, the spin tests were conducted in a manner that would not be affected by the vibration characteristics of the assembly, taking into account the rotordynamic effects in the layout.

5. Conclusions

In this study, rotordynamic analyses were conducted using a Simulink tool developed with a discrete model approach. The results obtained from the Simulink tool were initially validated using two-dimensional modal analyses. The primary reason for using two-dimensional modal analyses in the preliminary phase was to achieve quick results by employing a low mesh element count. Following the integration of both the 4 kg and 10 kg test specimens into the system, modal analyses were performed using the finite element method in both two and three dimensions, and the results were compared with the Simulink outputs.

For the 10 kg test specimen, the largest discrepancy between finite element analysis and Simulink results was calculated as 4.4% for the first bending mode and 0.73% for the second bending mode. A detailed comparison between the finite element analysis and Simulink results was also performed for the 4 kg test specimen. The largest deviations were found to be 2.12% for the first bending mode, 5.6% for the first torsional mode, and 4.96% for the second bending mode. It was determined that the Simulink model produced consistent results with finite element methods. However, in two-dimensional analyses, the error rates increased for test specimens with reduced cylindrical symmetry, which was expected. The error rates calculated for the three-dimensional analyses, which accounted for asymmetric cross sections, were found to be lower. The primary reason for the discrepancies in the calculations can be attributed to the geometric simplifications employed in the Simulink model. When comparing the Simulink results with impact tests, the largest discrepancies were observed as 4.2% for the first bending mode of the 10 kg test specimen and 4.85% for the 4 kg test specimen.

By employing the discrete model built in the Simulink environment, alternating stress due to vibration can be mitigated at the tested speeds during the preliminary design phase, thereby allowing the completion of the rotordynamic layout. In this model, the bearing stiffness and damping values that affect rotordynamics are parameterized to determine the

optimal bearing selection and the required stiffness and damping values, which enables spin tests to be conducted at vibration-free speed limits, ensuring the most accurate results.

Author Contributions: Investigation, Mert Uğur; Supervision, Osman Kopmaz. All authors have read and agreed to the published version of the manuscript.

Funding: This research received no external funding.

Institutional Review Board Statement: Not applicable.

Informed Consent Statement: Not applicable.

Data Availability Statement: The original contributions presented in the study are included in the article, further inquiries can be directed to the corresponding author.

Conflicts of Interest: The authors declare no conflict of interest.

References

1. Xie, Y.H.; Liu, Q.; Zhu, S.P.; Sun, H.; He, Y.; Wang, Q. Burst speed prediction and reliability assessment of turbine disks: Experiments and probabilistic aspects. *Eng. Fail. Anal.* **2023**, *145*, 107053. [CrossRef]
2. Sharma, J.; Tiwari, I.; Parmananda, P.; Rivera, M. Aperiodic bursting dynamics of active rotors. *Phys. Rev. E* **2022**, *105*, 014216. [CrossRef]
3. Sarıten, A.; Tabakçı, B.; Çopur, F.; Kutmaral, A.; Akpınar, İ.H. Burst speed prediction of impellers with critical strain criteria. *J. Eng. Gas Turbines Power* **2024**, *146*, 021003. [CrossRef]
4. Briend, Y.; Chatelet, E.; Dufour, R.; Andrianoely, M.A.; Legrand, F.; Sousa, M.S., Jr.; Steffen, V., Jr.; Baudin, S. Dry-whip phenomenon in on-board rotordynamics: Modeling and experimentation. *J. Sound Vib.* **2021**, *513*, 116398. [CrossRef]
5. Hartl, S.; Schulz, A.; Sima, H.; Koch, T.; Kaltenbacher, M. A static burst test for composite flywheel rotors. *Appl. Compos. Mater.* **2016**, *23*, 271–288. [CrossRef]
6. Xu, J.; Qiao, B.; Liu, M.; Yang, Z.; Chen, X. Crack propagation monitoring of rotor blades using synchroextracting transform. *J. Sound Vib.* **2021**, *509*, 116253. [CrossRef]
7. Xie, Z.; Yang, K.; He, T.; Jiao, J. Experimental and theoretical analysis on the nonlinear rotor-dynamic performances and vibration characteristics of a novel bearing-rotor system. *Mech. Syst. Signal Process.* **2023**, *199*, 110416. [CrossRef]
8. Huang, X.; Chen, C.; Xuan, X.; Guo, X.; Shan, X.; Hong, W. Fatigue crack propagation analysis in an aero-engine turbine disc using computational methods and spin test. *Theor. Appl. Fract. Mech.* **2023**, *124*, 103745. [CrossRef]
9. Zhu, H.M.; Chen, W.F.; Zhu, R.P.; Zhang, L.; Gao, J.; Liao, M.J. Dynamic analysis of a flexible rotor supported by ball bearings with damping rings based on FEM and lumped mass theory. *J. Cent. South Univ.* **2020**, *27*, 3684–3701. [CrossRef]
10. Meng, Z.S.; Peng, H.; Xie, Y.Y. Analysis of the dynamic load characteristics of double-top-beam supports with gaps. *Int. J. Simul. Model.* **2023**, *22*, 291–302. [CrossRef]
11. Zhou, Q.H.; Qiu, Y.; Liu, H.S.; He, Y. A performance study on structural parameters of centre-axle-trailer combinations. *Int. J. Simul. Model.* **2023**, *22*, 168–179. [CrossRef]
12. Kim, B.J.; Oh, J.; Palazzolo, A. Contact Interface Damping Effect on Internal Friction and Rotordynamic Instability. *J. Sound Vib.* **2024**, *592*, 118629. [CrossRef]
13. Hiroshima, N.; Hatta, H.; Yoshimura, J.; Goto, K.; Kogo, Y.; Wakayama, S. Stiffness degradation effects on disk-shaft connection behavior of a three-dimensionally carbon-fiber-reinforced composite rotating disk. *Compos. Struct.* **2020**, *234*, 111660. [CrossRef]
14. D'Souza, K.; Kurstak, E.; Ruff, K.; Dunn, M.G. A new experimental facility for characterizing bladed disk dynamics at design speed. *AIAA J.* **2020**, *58*, 2682–2690. [CrossRef]
15. Kurstak, E.; D'Souza, K. Experimental Investigation of Bladed Disk Dynamics at Design Speed under Synchronous Vibration. *AIAA J.* **2021**, *59*, 4123–4133. [CrossRef]
16. Buchroithner, A. Rotors for Mobile Flywheel Energy Storage. In *Flywheel Energy Storage: In Automotive Engineering*; Springer: Wiesbaden, Germany, 2023; pp. 129–182. [CrossRef]
17. Hu, D.; Dai, X.; Li, W.; Zhu, Y.; Zhang, X.; Chen, H.; Zhang, Z. A review of flywheel energy storage rotor materials and structures. *J. Energy Storage* **2023**, *74*, 109076. [CrossRef]
18. Zhang, Y.; Wang, W.; Wei, D.; Wang, G.; Xu, J.; Liu, K. Dynamic stability of unbalance-induced vibration in a turbocharger rotor-bearing system with the nonlinear effect of thermal turbulent lubricating fluid film. *J. Sound Vib.* **2022**, *528*, 116909. [CrossRef]
19. Guo, Y.; Liu, Y.X.; Wu, Y.W.; Cao, H.; Mo, D. Design optimization and burst speed prediction of a Ti2AlNb blisk. *Int. J. Aerosp. Eng.* **2021**, *2021*, 3290518. [CrossRef]
20. Kim, S.; Shin, D.; Palazzolo, A.B. A review of journal bearing induced nonlinear rotordynamic vibrations. *J. Tribol.* **2021**, *143*, 111802. [CrossRef]
21. Shin, D.; Yang, J.; Tong, X.; Suh, J.; Palazzolo, A. A review of journal bearing thermal effects on rotordynamic response. *J. Tribol.* **2021**, *143*, 031803. [CrossRef]

22. Zhang, Y.; He, Z.; Liu, C.; Wang, M.; Xuan, H.; Qu, M.; Fang, Z. Research on the explosion release method and damage mechanism of titanium alloy fan blade. *J. Mech. Sci. Technol.* **2023**, *37*, 4025–4037. [CrossRef]
23. Ali, M.S.; Mortazavi, F.; Palazzolo, A. Flow Field Instability and Rotordynamic Impedances for an Open Impeller Centrifugal Pump in Transient Four-Quadrant Regimes. In *Turbo Expo: Power for Land, Sea, and Air*; American Society of Mechanical Engineers: Houston, TX, USA, 2020; Volume 84225, p. V10BT29A009. [CrossRef]
24. Kim, B.J.; Oh, J.; Palazzolo, A. An improved preloaded Curvic coupling model for rotordynamic analyses. *J. Sound Vib.* **2023**, *544*, 117391. [CrossRef]
25. Cosco, F.; Serratore, G.; Catera, P.G.; Gagliardi, F.; Luberto, E.; Mundo, D. Experimental assessment of stiffness and energy dissipation properties of disk-shaped polymer-based composite specimens by in-plane torsion testing. *Polym. Test.* **2020**, *83*, 106351. [CrossRef]
26. Xie, Z.; Yang, K.; Gao, W.; Zhao, B.; Du, P.; Zhang, M. Rotor dynamic behaviors of a novel bearing system with bi-directional tilting effects: Experiment and theory. *Mech. Syst. Signal Process.* **2024**, *220*, 111675. [CrossRef]
27. Li, B.; Cui, Y.; Liu, S.; Liu, Y.; Wang, X.; Ding, Z. Experimental and numerical study based on ductile failure for the tri-hub burst of turbocharger turbine. *Eng. Fail. Anal.* **2022**, *138*, 106295. [CrossRef]
28. Garoli, G.Y.; Pilotto, R.; Nordmann, R.; de Castro, H.F. Identification of active magnetic bearing parameters in a rotor machine using Bayesian inference with generalized polynomial chaos expansion. *J. Braz. Soc. Mech. Sci. Eng.* **2021**, *43*, 552. [CrossRef]
29. Ferede, E.; Gandhi, F. Aeroelastic load analysis of a co-rotating quad-rotor wind turbine. *Wind. Energy* **2022**, *25*, 450–467. [CrossRef]
30. Ayyadevara, N.T.; Subramanian, B.; Meda, N.S. Experimental and Computational Investigation for Accelerated Testing and Characterization of Next-Generation Steam Turbine Rotors. *J. Therm. Sci. Eng. Appl.* **2022**, *14*, 121011. [CrossRef]
31. Zhang, S.; Lu, Y.; Qiu, Z.; Hu, W.; Dong, Z.; Qiu, Z.; Qiu, Y. Distance Measurement of Contra-Rotating Rotor Blades with Ultrasonic Transducers. *Micromachines* **2024**, *15*, 676. [CrossRef]
32. Tang, C.L.; Dai, X.J.; Zhang, X.Z.; Jiang, L. Rotor dynamics analysis and experiment study of the flywheel spin test system. *J. Mech. Sci. Technol.* **2012**, *26*, 2669–2677. [CrossRef]
33. Buchroithner, A. Flywheel Energy Storage Housing. In *Flywheel Energy Storage: In Automotive Engineering*; Springer: Wiesbaden, Germany, 2023; pp. 183–225. [CrossRef]
34. *ISO 21940-11:2016*; Mechanical Vibration—Rotor Balancing. ISO: Geneva, Switzerland, 2016.

Disclaimer/Publisher's Note: The statements, opinions and data contained in all publications are solely those of the individual author(s) and contributor(s) and not of MDPI and/or the editor(s). MDPI and/or the editor(s) disclaim responsibility for any injury to people or property resulting from any ideas, methods, instructions or products referred to in the content.